INFILTRATION OF POROUS ULTRA-HIGH TEMPERATURE CERAMICS FOR ACTIVE COOLING

Aliya Kaplan and Dr. Carolina Tallon
Department of Materials Science and Engineering, Advanced Manufacturing Team, Virginia Polytechnic Institute and State University, Blacksburg, VA 24061

Abstract

Space and hypersonic travel create extreme thermal and ablative conditions which most materials cannot survive. Ultra-high temperature ceramics (UHTCs) are unique in their high melting temperatures, thermal resistance, and mechanical strength, giving them better odds against these extreme conditions. Past thermal protection systems (TPS) have relied on polymer-based heat sinks or sacrificial materials to protect critical components of the aircraft. These TPS may not be able to survive the extreme temperatures that new hypersonic designs require. With recent developments in the manufacturing processes of UHTCs, interest in UHTC-based TPS and active cooling strategies has grown. The goal of this work was to develop homogenous aligned porous structures in UHTC materials using ice templating. Samples with up to 70% porosity and pore sizes ranging from 5 to 17 μm, aligned longitudinally to the axis were prepared by controlling the freezing front formation at -80°C at various solid loadings. The microstructure was characterized using SEM and the porosity connectivity was assessed using infiltration of a liquid phase. The effect of porosity on the mechanical properties of UHTCs was assessed both experimentally and computationally.

Introduction

Space and hypersonic travel produce extreme thermal and ablative conditions which most materials cannot survive. Thermal protection systems (TPS) have been designed to take the brunt of the thermal and ablative load during hypersonic and space re-entry flights. Most past TPS have relied on polymeric heat sinks and sacrificial materials which degrade quickly under extreme flight conditions, and thus, do not meet the growing demand for higher temperature survivability at higher aircraft speeds and hypersonic conditions.[1,2]

Ultra-high temperature ceramics (UHTCs) are unique in their high melting temperatures, thermal resistance, and mechanical strength, making them suitable candidate materials for some of the key components of hypersonic and space vehicles such as the leading edges, combustor, and insulation.[3,4,5,6,7] Restrictions in the manufacturing of UHTCs to develop complex microstructures and architectures has limited their wider use in TPS in the past. However, in the last ten years, advancements have been made in colloidal processing of these materials such that their microstructures and architectures can now be tailored to enable more complex strategies for TPS, including active cooling approaches.[8]

Aligned multi-scale porosity in UHTC materials is a new microstructure of interest in the development of active cooling approaches.[9] The hypothesis is that the aligned porous structure will favor the flow of heat along the pore axis and restrict the flow of heat perpendicular to the pore axis allowing heat to be directed out of the aircraft, to protect any components more sensitive to high thermal loads.[9] With connected aligned porosity, the material can be infiltrated with a secondary phase, contributing to heat removal by different mechanisms such as conduction, convection, radiation, evaporation and/or ablation. The cooling of UHTC materials via the circulation of another phase through their porous structures would enhance the performance of these materials for their applications in the aerospace industry, allowing these aircrafts to stand up to faster and farther travel than ever before.

This aligned multi-scale porosity in UHTCs can be developed via ice templating. Ice templating is a colloidal processing route involving the quick freezing of a suspension such that the frozen solvent acts as a binder for the ceramic particles.[8,10,11] The frozen sample can then be demolded without damage to the green body and the frozen solvent is sublimated away to leave behind the final green body. Ice templating can be used to develop dense and porous UHTC materials, but this paper will focus on the use of ice templating in creating aligned porosity. To create aligned porosity using ice templating, the heat flux out of the suspension must be directional upon freezing. Vertical alignment is developed by freezing UHTC suspensions on an ultra-cold aluminum block at ambient temperature. When the heat flux is directed out through the bottom of the suspension, solvent crystals form vertically and the ceramic particles in the suspension are pushed between the channels of ice. Freezing temperature and solid content of the suspension have significant effects on the microstructure of the resulting material.

This paper explores the creation of aligned multi-scale porous UHTC materials via ice-templating for the purpose of developing new infiltration-based active cooling strategies. The first step in developing this new active cooling approach is taken in this study. The

microstructure of these materials was characterized, connectivity of the pores was validated, and the effect of porosity on the mechanical properties of UHTCs was investigated both experimentally and computationally.

Experimental Procedure

Materials

Zirconium diboride (ZrB_2 Grade B, Hoganas, Germany) was the ceramic powder used in this work. Cyclohexane (anhydrous, 99.5%, Sigma Aldrich, St. Louis, MO) was used as the solvent and Hypermer A70 (CRODA, East Yorkshire, UK) was used as the particle dispersant. Suspensions of ZrB_2 in cyclohexane were produced with solid contents of 20 and 30 vol% and in batch volumes of 25 mL each. The quantity of dispersant in each batch was measured to be 1 wt% with respect to the weight of ceramic powder. Suspension preparation first involved dissolving the dispersant in the solvent, then adding in the ceramic powder, and finally sonicating the suspension to suspend ceramic particles in the suspension. The sonication procedure is described in the following section.

Ice Templating

Ice templating was employed in this experiment to develop a vertically aligned porous structure within the ceramic coupons. Figure 1 visually describes the steps involved in the ice-templating procedure. First, cylindrical coupon molds (internal diameter of 23.1 mm and height of 25.6 mm) were prepared. To ensure ease of demolding, stainless steel cylinders and plates were coated with Krytox grease. Then, the gap between the cylinder and plate was sealed with Play-Doh to avoid leaks.

Once molds were prepared, suspensions of ZrB_2 were sonicated using an ultrasonic homogenizer (FB705, Fisher Scientific, Pittsburgh, PA) for two minutes with one second pulses. While sonication occurred, a frozen aluminum block (51x51x76 mm) was removed from the low-temperature freezer (85-1.7A, ScienTemp, Adrian, MI) set to -80 °C and placed on the lab bench. Molds were placed directly on top of the aluminum block. Immediately after sonication was complete, suspensions were poured into the molds and allowed to freeze completely before returning the aluminum block and frozen coupons to the freezer. Coupon freezing took approximately 5 minutes, but there was variation in freezing time depending on solid content amount and placement of the mold on the aluminum block. These steps were completed in quick succession to avoid warming of the aluminum block and any settling of the ZrB_2 particles.

With even pressure on the surface of the frozen coupons, coupons were gently demolded and immediately returned to the freezer to prevent melting. Using the tabletop freeze dryer (FreeZone$^{2.5Plus}$, LABCONCO, Kansas City, MO), frozen cyclohexane was sublimated from the coupons (diameter of 23.7 mm and height of 24.5 mm). The freeze dryer was run for 24-48 hours for all samples.

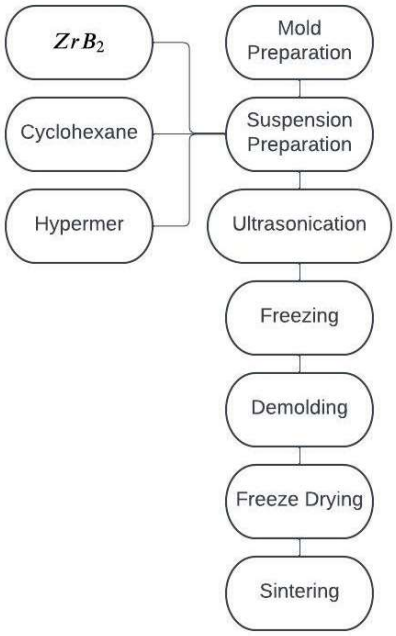

Fig. 1. Flow chart of the ice templating process.

Sintering

Green bodies were sintered in a vacuum furnace (Red Devil, R. D. WEBB, Natick, MA) with graphite heating element, spacers, and crucible. First, the furnace ramped to a temperature of 400°C at 5°C/min and then dwelled at that temperature for 60 minutes to remove the organic dispersant and any remainder of solvent. The next ramp went up to a temperature of 1500°C at a rate of 5°C/min and then dwelled there for 10 minutes to allow for the switching between thermocouple and pyrometer. The final upwards ramp at a rate of 3°C/min reached a temperature of 1800°C where argon was backfilled into the furnace. This temperature ramp continued to a maximum temperature of 2000°C where the furnace dwelled for 60 minutes. Then, the furnace ramped back down to 1500°C at 3°C/min before dwelling for 10 minutes (to switch back from pyrometer to thermocouple and turn off argon flow). Finally, the furnace ramped down to 800°C at 10°C/min and was left to cool to room temperature overnight before unloading.

Characterization

The development of the aligned porous structure was validated using scanning electron microscopy (SEM) and vacuum infiltration.

Density

The Archimedes method was used to measure green and sintered density of UHTC coupons. The Archimedes

method involves placing a scale on an elevated surface and hanging a basket and hook from the under part of the scale such that the basket is fully immersed in water. For green samples, dry weight was taken first on the top scale balance, then the sample was coated with melted wax (density of 0.81 g/cm^3) and weighed again on the top scale balance, and finally the wet weight of the sample was measured in the basket. Green density of the sample was then calculated using Equation (1)

$$\rho_s = \frac{DryWT_s}{\frac{DryWT_{s+w} - WetWT_{s+w}}{\rho_l} - \frac{DryWT_w}{\rho_w}} \quad (1)$$

where $DryWT_s$ is dry weight of the sample, $DryWT_{s+w}$ is dry weight of the sample coated in wax, $WetWT_{s+w}$ is wet weight of the sample coated in wax, $DryWT_w$ is dry weight of the wax, ρ_l is density of the liquid, and ρ_w is density of the wax.

Sintered samples were soaked in water for 3-4 days prior to measurement. Once fully saturated with water, the wet weight of the sample was measured in the basket. Then, the sample surface was dried with a Kimwipe and the saturated sample was measured on the top scale balance. Samples were then dried overnight to remove all water and the dry weight was measured the next day. Sintered density of the sample was then calculated using Equation (2)

$$\rho_s = \frac{DryWT_s}{SatWT_s - WetWT_s}\rho_l \quad (2)$$

where $DryWT_s$ is dry weight of the sample, $SatWT_s$ is saturated weight of the sample, $WetWT_s$ is wet weight of the sample, and ρ_l is density of the liquid.

Scanning Electron Microscopy

A JEOL IT500 SEM was used to capture images of pore alignment in ice templated UHTCs as well as measure pore size in sintered UHTC coupons with solid content loadings of 20 and 30 volume percent.

Vacuum Infiltration

Infiltration of the aligned porous structure in UHTC coupons with deionized water was performed using the modified vacuum infiltration rig seen in Figure 2. As seen in Figure 2b, the reservoir was filled with deionized water to just below the UHTC coupon which was placed on a mesh stand. A water valve was turned on allowing the aspirator pump to pull vacuum within the reservoir. Vacuum pressure reached up to -57 kPa and infiltrations occurred for durations of 5 and 10 minutes.

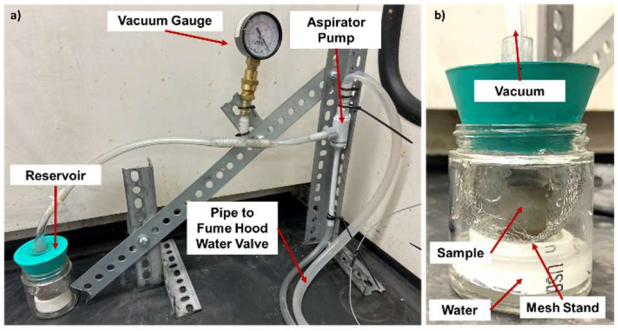

Fig. 2. a) Infiltration rig. b) Reservoir close-up.

Compressive Strength Testing

An Instron 5969 with a 50 kN load cell was used for compressive strength testing. Samples were loaded onto the compression set up with two parallel plates. During testing, strain was measured using crosshead displacement, and load was measured using the attached load cell.

Results and Discussion

Microstructure

Green density and sintered density measurements were taken for all samples while pore size was measured for sintered samples only. Table 1 shows average green and sintered porosity as well as average pore size for UHTC coupons of 20 and 30 volume percent. As expected, percent porosity decreases as solid content increases. Sintering also decreases the percent porosity of all samples. The pore size of the relatively large ice-templating pores can be seen in Table 1 as well as in Figures 3a and 3b. These two images indicate that pore size decreased with an increase in solid content loading.

While ice-templating produces large/pronounced pores, interparticle porosity is also present. Figure 3c shows an SEM image of a green 30 vol% ZrB_2 sample and Figure 3d shows a sintered 30 vol% ZrB_2 sample. Sintering removes most interparticle porosity present in green samples. The densification is not complete, so there is a certain degree of interparticle porosity in the struts of the porous sample. This interparticle porosity is used to further tailor the thermal conductivity of the samples.

There is little reported pore size and porosity data for ice-templating with cyclohexane. Literature reporting pore size and porosity data for ice-templating using cyclohexane only studies suspensions with higher solid content loadings (50 vol%) than those prepared in this study.[12] However, the values in Table 1 are comparable to values in the literature for ice-templating using camphene and *tert*-Butyl alcohol (TBA). Ice-templating with camphene and TBA show porosity ranges of 60-80% for 20 vol% solid content loading and 40-65% for 30 vol % solid content loading respectively.[13] While these porosity ranges are large, the data collected in this experiment falls within these limits.

Table 1. Summary of sample porosities and pore sizes.

Vol %	Green Porosity (%)	Sintered Porosity (%)	Pore Size (μm)
20	73.95 ± 1.5	65.1 ± 2.0	14.1 ± 3.4
30	63.73 ± 5.9	48.6 ± 2.8	6.44 ± 1.7

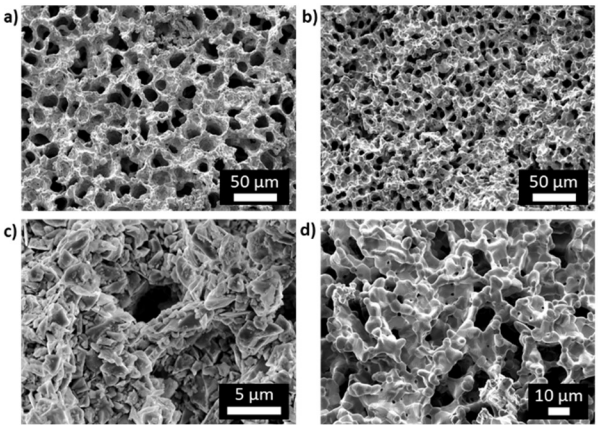

Fig. 3. SEM of interparticle porosity in ice-templated zirconium diboride. a) Sintered, 20 vol%. b) Sintered, 30 vol%. (c) Green, 30 vol%. d) Sintered, 30 vol%.

To verify the success of developing aligned porosity in UHTC coupons, SEM imaging was performed on sintered samples that were sectioned such that the cross-sections perpendicular and parallel to the freezing direction were visible. Figure 4 below shows the parallel cross-section (left) and perpendicular cross-section (right). As seen in Figure 4, the parallel cross-section shows circle-shaped pores indicating a majority of frozen cyclohexane crystals grew in the vertical direction. Further indicating alignment is the image of the perpendicular cross-section which shows vertical orientation of the pores.

Validating Porous Alignment and Connectivity

Vacuum infiltration of 30 vol% ZrB_2 coupons was performed to further confirm that pores were developed with alignment and there is connectivity across the entire cross-section. Figure 5a shows the water mass gain for each infiltration test as well as the maximum amount of water possible to gain which was calculated using the measured percent porosity of the samples infiltrated. As seen in Figure 5a, infiltration duration has little effect on

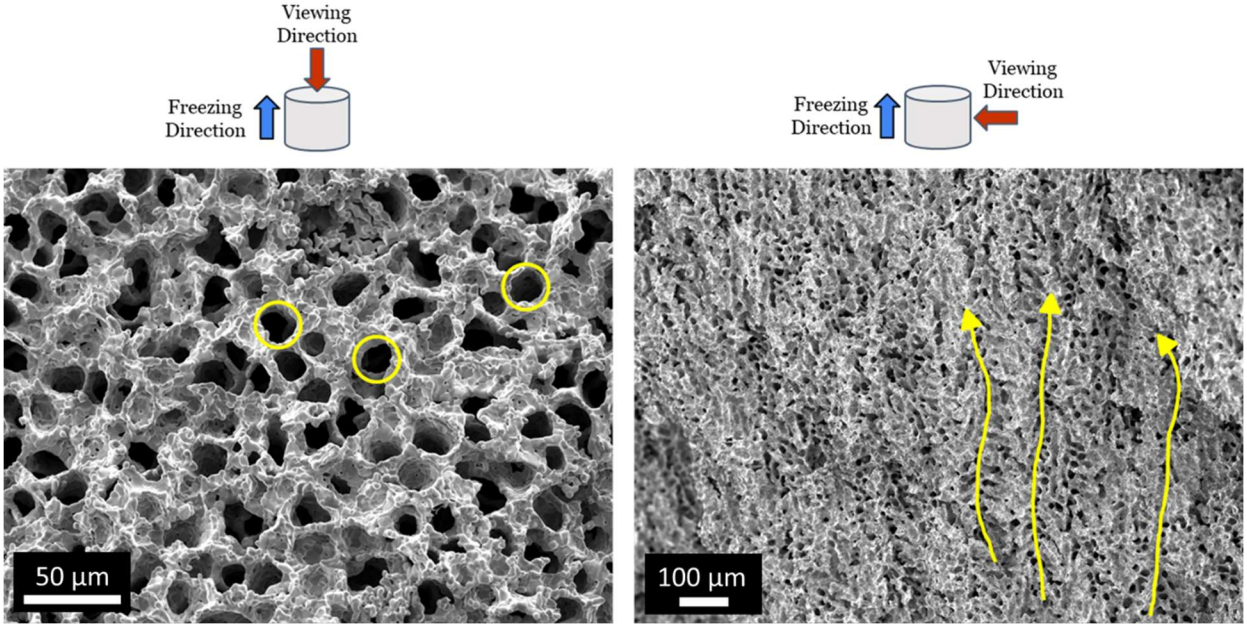

Fig. 4. SEM of aligned porous structure in ice-templated zirconium diboride. (Left) Viewing direction is perpendicular to the ice propagation direction. (Right) Viewing direction is parallel to the ice propagation direction.

the water gained during each test. Additionally, it is worth noting that the tests where water was not gained may have been a result of the water in the reservoir not being close enough to the sample prior to pulling vacuum. However, by showing that water successfully infiltrated the UHTC coupons up to a value close to the total porosity in the sample there is verification that an aligned porous structure was achieved.

Furthermore, the mass of each sample was measured at various times after each infiltration test as seen in Figure 5b. The purpose of these measurements was to understand how quickly the infiltrating phase is lost from the porous microstructure (first steps towards understanding tortuosity of the porous structures). In future experiments, suspensions of particles in water may be used as the infiltrating phase and it will be important to understand how much time there is to retain the particles within the pores before they are lost due to draining. As seen in Figure 5b, water was lost at a faster rate from the sample infiltrated for 10 minutes than the samples infiltrated for 5 minutes.

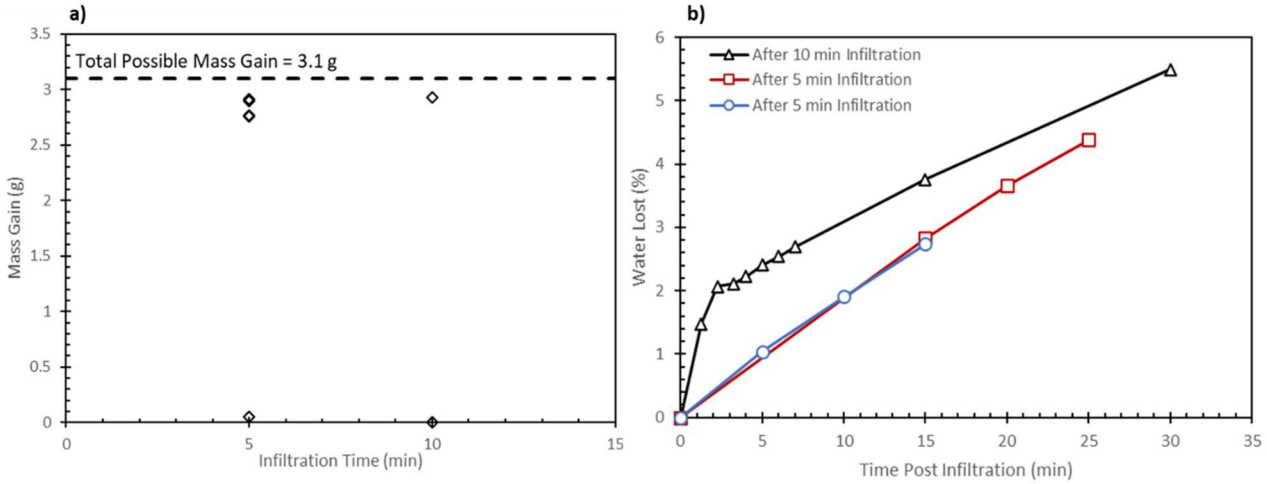

Fig. 5. a) Water mass gain for infiltration times of 5 and 10 minutes. Note that the approximate total possible mass gain is 3.1 grams. b) Rate of water loss post-infiltration of aligned pores.

Mechanical Properties

A limited number of samples without visible flaws were made, and thus, there are few compressive strength data sets for ice-templated coupons. Figure 6 shows the compressive strength data that was collected, and Table 2 summarizes the resulting compressive strength and strain at fracture values for each test. Relative to values in the literature, the compressive strength values in Table 2 are particularly low, even when factoring in the porosity of the samples. Also, stress-strain curves for porous ceramics in the literature appear to continue on-to much larger strains before an overall drop in stress is seen. It is likely that the tests seen in Figure 6 were stopped too early as the drop in stress at the end of each run was believed to mean the samples had broken when in fact, these drops are simply a result of the failure of some struts within the samples. If these runs had continued, there likely would have been a larger measured compressive strength for both 20 and 30 vol% samples, based on previous experience with similar microstructures. More compressive strength experiments will need to be completed to address these unknowns.

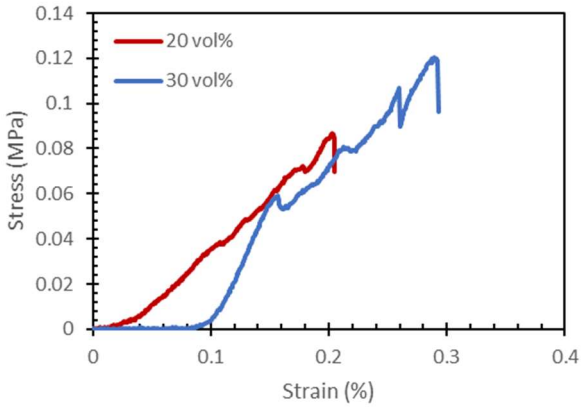

Fig. 6. Stress-strain curves for aligned porous UHTCs at solid content loadings of 20 and 30 vol%.

Table 2. Summary of compressive strength data.

Vol %	Compressive Strength (MPa)	Strain at Fracture (%)
20	0.09	0.20
30	0.12	0.29

Gibson and Ashby's model for crushing strength of brittle foams was used to approximate the predicted compressive strength values for aligned porous ZrB_2 as a function of percent porosity in Python. Equation (3)

$$\frac{\sigma_f^*}{\sigma_f} = C_7 \left(\frac{\rho}{\rho_s}\right)^{3/2} \quad (3)$$

shows the Gibson-Ashby brittle crushing equation where σ_f^* is the compressive strength of the porous material, σ_f is the compressive strength of the cell wall material, C_7 is a dimensionless constant, ρ is the density of the porous material, and ρ_s is the density of the cell wall material.[14] This equation is seen plotted in Figure 7 as the dark blue curve and the fitted white data points are literature values compiled by Gibson and Ashby. Also present in Figure 7 is the green data point representing compressive strength data of ice-templated ZrB_2 collected previously by the Tallon Research Group. Compressive strength values from Table 1 were plotted versus percent porosity seen as the red data points in Figure 7. Clearly, the curve generated by (3) predicts much higher values of compressive strength for aligned porous ZrB_2 than the ones achieved during compressive strength testing in this study. However, compressive strength data collected previously by the Tallon Research Group appears to fit the original Gibson-Ashby model quite well. Thus, two things can be recognized here. The constant, C_7 in (3) can be modified to give the model a better fit to the experimental data collected in this study (light blue curve in Figure 7), but this is limited by the few numbers of data points. The other option is to recognize that both completed compressive strength tests likely ended too early and the values in Table 2 are inaccurate. Thus, Figure 7 further indicates the need for more compressive strength testing in future experiments.

Conclusions

This study took strides towards developing a new infiltration-based active cooling approach utilizing porously aligned ZrB_2. Longitudinally aligned porous samples showed porosities up to 70% and pore sizes ranging from 5 to 17 µm for solid content loadings of 20 and 30 vol%. Connectivity of the aligned pores was confirmed by the water mass gained during vacuum infiltration experiments. Minimum water loss in the first thirty minutes post-infiltration shows promise with regard to retaining infiltrating particles within the sample microstructure. While high porosity leads to good infiltration of the porous network, resulting mechanical properties will decrease. Future work must involve further compressive strength tests as data is unreliable and limited. Additionally, thermal characterization of the samples to determine the thermal conductivity along and across the pore axis will be conducted. This work represents the first step in the study of aligned porous UHTCs for active cooling applications. Future studies will also investigate infiltration of the porous structures with various fluids and other solid phases as well as quantification of heat removal in each of those cases.

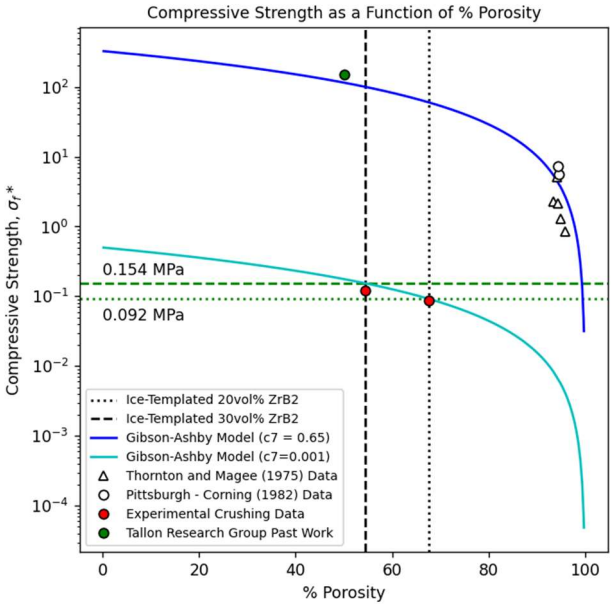

Fig. 7. Model of the mechanical behavior of aligned porous UHTCs. Dark blue line displays the Gibson-Ashby model for brittle crushing and red compressive strength data points are from the literature. Green data point is experimental data collected by the Tallon research group. Light blue line displays the modified Gibson-Ashby model which fits the compressive strength data collected in this experiment.

Acknowledgements

Aliya Jordan Kaplan acknowledges the Virginia Space Grant Consortium for the financial support of this project via the Undergradute Scholarship Program. The authors also acknowledge the Department of Materials Science and Engineering at Virginia Tech, as well as Kaitlyn Shirey, Julia N. Goyer, Juan Diego Shiraishi Lombard, and Hannah Blaha from the Tallon Research Group at Virginia Tech for their assistance in this work.

References

[1] O. Uyanna and H. Najafi, "Thermal protection systems for space vehicles: A review on technology development, current challenges and future prospects," Acta Astronautica, vol. 176, pp. 341–356, Nov. 2020, doi: 10.1016/j.actaastro.2020.06.047.

[2] V. T. Le, N. S. Ha, and N. S. Goo, "Advanced sandwich structures for thermal protection systems in hypersonic vehicles: A review," Composites Part B: Engineering, vol. 226, p. 109301, Dec. 2021, doi: 10.1016/j.compositesb.2021.109301.

[3] C. Tallon, S. Slater, A. Gillen, C. Wood, J. Turner, “Ceramic materials for hypersonic applications,” Materials Australia, June, p. 28-32, 2011.

[4] R. Djugum, K. Sharp, “The fabrication and performance of C/C composites impregnated with TaC filler,” Carbon, vol. 115, pp. 105-115, 2017, doi: 10.1016/j.carbon.2016.12.019.

[5] C. Hong, J. Han, X. Zhang, S. Meng, S. Du, “Thermal ablation resistance of melt-infiltrated titanium diboride-(copper, nickel) composites,” Journal of Alloys and Compounds, 2007. [Online].

[6] M. M. Opeka, I. G. Talmy, E. J. Wuchina, J. A. Zaykoski, and S. J. Causey, “Mechanical, Thermal, and Oxidation Properties of Refractory Hafnium and zirconium Compounds,” *Journal of the European Ceramic Society*, vol. 19, no. 13, pp. 2405–2414, Oct. 1999, doi: 10.1016/S0955-2219(99)00129-6.

[7] W. G. Fahrenholtz, G. E. Hilmas, I. G. Talmy, and J. A. Zaykoski, “Refractory Diborides of Zirconium and Hafnium,” *Journal of the American Ceramic Society*, vol. 90, no. 5, pp. 1347–1364, 2007, doi: 10.1111/j.1551-2916.2007.01583.x.

[8] G. V. Franks, C. Tallon, A. R. Studart, M. L. Sesso, and S. Leo, "Colloidal processing: enabling complex shaped ceramics with unique multiscale structures," Journal of the American Ceramic Society, vol. 100, no. 2, pp. 458-490, 2017, doi: 10.1111/jace.14705.

[9] D. C. Hicks, Z. Zhou, G. Liu, C. Tallon, “Aligned continuous cylindrical pores derived from electrospun polymer fibers in titanium diboride,” Applied Ceramic Technology, 2019. [Online]. Available: http://hdl.handle.net/10919/99423.

[10] C. Tallon and G. V. Franks, “Recent trends in shape forming from colloidal processing: A review,” *Journal of the Ceramic Society of Japan*, vol. 119, no. 1387, pp. 147–160, 2011, doi: 10.2109/jcersj2.119.147.

[11] E. Landi, D. Sciti, C. Melandri, and V. Medri, “Ice templating of ZrB2 porous architectures,” *Journal of the European Ceramic Society*, vol. 33, pp. 1599–1607, Sep. 2013, doi: 10.1016/j.jeurceramsoc.2013.01.037.

[12] S. Leo, L. Jukes, S. Pinches, C. Tallon, and G. V. Franks, “Freeze casting for near-net-shaping of dense zirconium diboride ceramics,” *Journal of the American Ceramic Society*, vol. 101, no. 7, pp. 2770–2785, 2018, doi: 10.1111/jace.15451.

[13] S. Deville, S. Meille, and J. Seuba, “A meta-analysis of the mechanical properties of ice-templated ceramics and metals,” *Sci Technol Adv Mater*, vol. 16, no. 4, p. 043501, Jul. 2015, doi: 10.1088/1468-6996/16/4/043501.

[14] M. F. Ashby and R. F. M. Medalist, “The mechanical properties of cellular solids,” MTA, vol. 14, no. 9, pp. 1755–1769, Sep. 1983, doi: 10.1007/BF02645546.